nature COMMUNICATIONS

ARTICLE

Received 14 Aug 2012 | Accepted 12 Dec 2012 | Published 29 Jan 2013

DOI: 10.1038/ncomms2375

Composite-pulse magnetometry with a solid-state quantum sensor

Clarice D. Aiello[1], Masashi Hirose[1] & Paola Cappellaro[1]

The sensitivity of quantum magnetometer is challenged by control errors and, especially in the solid state, by their short coherence times. Refocusing techniques can overcome these limitations and improve the sensitivity to periodic fields, but they come at the cost of reduced bandwidth and cannot be applied to sense static or aperiodic fields. Here we experimentally demonstrate that continuous driving of the sensor spin by a composite pulse known as rotary-echo yields a flexible magnetometry scheme, mitigating both driving power imperfections and decoherence. A suitable choice of rotary-echo parameters compensates for different scenarios of noise strength and origin. The method can be applied to nanoscale sensing in variable environments or to realize noise spectroscopy. In a room-temperature implementation, based on a single electronic spin in diamond, composite-pulse magnetometry provides a tunable trade-off between sensitivities in the $\mu\mathrm{THz}^{-1/2}$ range, comparable with those obtained with Ramsey spectroscopy, and coherence times approaching T_1.

[1] Department of Nuclear Science and Engineering, Massachusetts Institute of Technology, 77 Massachusetts Avenue, Cambridge, Massachusetts 02139, USA. Correspondence and requests for materials should be addressed to P.C. (email: pcappell@mit.edu).

Solid-state quantum sensors attract much attention given their potential for high sensitivity and nano applications. In particular, the electronic spin of the nitrogen-vacancy (NV) colour centre in diamond is a robust quantum sensor[1–3] owing to a combination of highly desirable properties: optical initialization and readout, long coherence times at room temperature ($T_1 > 2$ ms (refs 4,5), $T_2 \gtrsim 0.5$ ms (ref. 6)), the potential to harness the surrounding spin bath for memory and sensitivity enhancement[7,8] and biocompatibility[9].

Magnetometry schemes based on quantum spin probes (qubits) usually measure the detuning $\delta\omega$ from a known resonance. The most widely used method is Ramsey spectroscopy[10], which measures the relative phase $\delta\omega t$ the qubit acquires when evolving freely after preparation in a superposition state. In the solid state, a severe drawback of this scheme is the short free-evolution dephasing time, T_2^*, which limits the interrogation time. Dynamical decoupling (DD) techniques, such as Hahn-echo[11] or Carr–Purcell–Meiboom–Gill[12] sequences, can extend the coherence time. Unfortunately, such schemes also refocus the effects of static magnetic fields and are thus not applicable for DC magnetometry. Even if $\delta\omega$ oscillates with a known frequency (AC magnetometry), DD schemes impose severe restrictions on the bandwidth, as the optimal sensitivity is reached only if the field period matches the DD cycle time[1]. Schemes based on continuous driving are thus of special interest for metrology in the solid state, because they can lead to extended coherence times[13]. Recently, DC magnetometry based on Rabi frequency beats was demonstrated[14]; in that method, a small detuning along the static magnetic field produces a shift $\approx(\delta\omega^2)/(2\Omega)$ of the bare Rabi frequency Ω. Despite ideally allowing for interrogation times approaching T_1, limiting factors such as noise in the driving field[14] and the bad scaling in $\delta\omega \ll \Omega$ make Rabi-beat magnetometry unattractive. More complex driving modulations[15] can provide not only a better refocusing of driving field inhomogeneities, but also different scalings with $\delta\omega$, yielding improved magnetometry. In this work, we use a novel composite-pulse magnetometry method as a means of both extending coherence times as expected by continuous excitation, and keeping a good scaling with $\delta\omega$, which increases sensitivity. The ϑ-rotary-echo (RE) is a simple composite pulse (Fig. 1a) designed to correct for inhomogeneities in the excitation field[16]; here, ϑ parametrizes the rotation angle of the half-echo pulse. For $\vartheta \neq 2\pi k$, $k \in \mathbb{Z}$, RE does not refocus magnetic fields along the qubit quantization axes and can therefore be used for DC magnetometry. For $\vartheta = 2\pi k$, RE provides superior decoupling from both dephasing[17–19] and microwave noise and can be used to achieve AC magnetometry[20].

Results

Dynamics under RE sequence. In the rotating frame associated with the microwave field, and applying the rotating wave approximation, the Hamiltonian describing a continuous stream of ϑ-REs is

$$\mathscr{H}(t) = \frac{1}{2}[\Omega \mathbb{SW}(t)\sigma_x + \delta\omega(\mathbb{1} - \sigma_z)], \qquad (1)$$

where $\mathbb{SW}(t) = \pm 1$ is the square wave of period $T = 2\vartheta/\Omega$. On resonance ($\delta\omega = 0$) the evolution is governed by the propagator $U_0 = e^{i\frac{\Omega}{2}\mathbb{TW}(t)\sigma_x}$, with $\mathbb{TW}(t)$ the triangular wave representing the integral of $\mathbb{SW}(t)$. We approximate the time evolution in the presence of a detuning $\delta\omega$ by a first-order Average Hamiltonian expansion[21] of equation (1), yielding an effective Hamiltonian over the cycle (Supplementary Methods)

$$\overline{\mathscr{H}}^{(1)} = -\frac{\delta\omega}{\vartheta}\sin\left(\frac{\vartheta}{2}\right)\left[\cos\left(\frac{\vartheta}{2}\right)\sigma_z - \sin\left(\frac{\vartheta}{2}\right)\sigma_y\right]. \qquad (2)$$

Extending the approximation in equation (2) to include the fast Rabi-like oscillations of frequency $\pi\Omega/(\vartheta \bmod 2\pi)$, we can thus

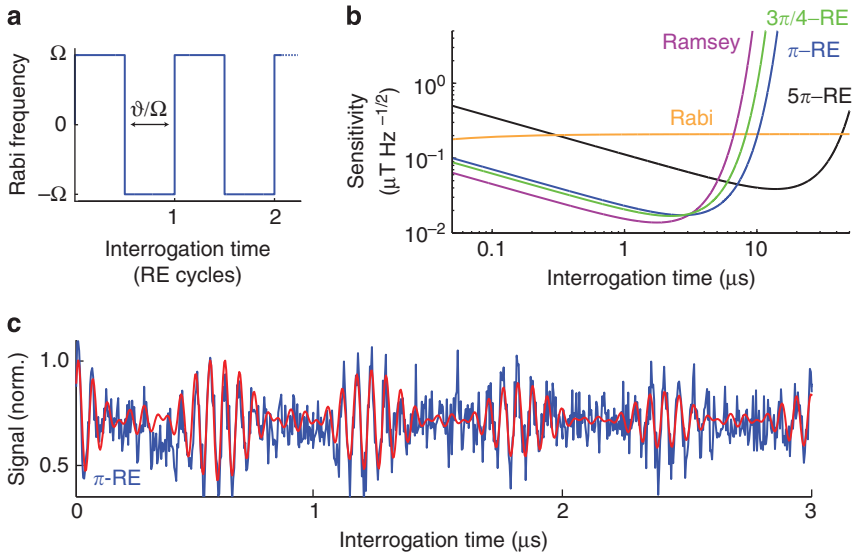

Figure 1 | RE magnetometry scheme and expected sensitivity. (**a**) Experimental control composed of a n-cycle ϑ-RE sequence, in which the phase of the microwave field is switched by π at every pulse of duration ϑ/Ω, where Ω is the Rabi frequency. (**b**) Magnetometry sensitivities η_{RE} of $\vartheta = \{3\pi/4, \pi, 5\pi\}$-RE sequences (green, blue, black), showing the tunability with the half-echo rotation angle. The sensitivity has its global minimum $\eta_{\mathrm{RE}} \approx 1.38/\sqrt{t}$ (comparable to Ramsey magnetometry, purple) for $\vartheta \approx 3\pi/4$ and consecutively increasing local minima for $\vartheta \approx (2k+1)\pi$. A decrease in sensitivity is followed by an increase in coherence time, which can approach T_1 as in Rabi-beat magnetometry (orange), whose sensitivity is limited by Ω. Sensitivities are simulated in the presence of static bath noise using parameters from the fit depicted in (**c**). (**c**) A typical normalized fluorescence signal after $n = 55$ RE cycles for $\vartheta = \pi$ and $\Omega \approx 2\pi \times 17$ MHz (blue); the modulation in the signal is due to the hyperfine interaction with the ^{14}N nucleus. The signal is filtered for even harmonics of $\pi\Omega/(\vartheta \bmod 2\pi)$ (Supplementary Methods) and then fitted to equation (3), modified to include decoherence induced by static bath noise (red).

calculate the population evolution for one of the qubit states,

$$\mathcal{S}(t) \approx \frac{1}{2}+\frac{1}{2}\cos^2\left(\frac{\vartheta}{2}\right)+\frac{1}{2}\sin^2\left(\frac{\vartheta}{2}\right) \times \cos\left(\frac{2\delta\omega t}{\vartheta}\sin\left(\frac{\vartheta}{2}\right)\right)\cos\left(\frac{\pi\Omega t}{(\vartheta \bmod 2\pi)}\right) \quad (3)$$

The signal $\mathcal{S}$ reveals the presence of two spectral lines at $\frac{\pi\Omega}{(\vartheta \bmod 2\pi)} \pm \frac{2\delta\omega}{\vartheta}\sin\left(\frac{\vartheta}{2}\right)$ for a detuning $\delta\omega$.

Sensitivity of the method. Thanks to the linear dependence on $\delta\omega$, we expect a favourable scaling of the sensitivity η, given by the shot-noise-limited magnetic field resolution per unit measurement time[1,22]. For N measurements and a signal standard deviation $\Delta\mathcal{S}$, the sensitivity is

$$\eta = \Delta B\sqrt{\mathcal{T}} = \frac{1}{\gamma_e}\lim_{\delta\omega\to 0}\frac{\Delta\mathcal{S}}{\left|\frac{\partial\mathcal{S}}{\partial\delta\omega}\right|}\sqrt{N(t+t_d)} \quad (4)$$

where γ_e ($\approx 2.8\,\mathrm{MHz G}^{-1}$ for NV) is the sensor gyromagnetic ratio and ΔB is the minimum detectable field. We broke down the total measurement time $\mathcal{T}$ into interrogation time t and the dead-time t_d required for initialization and readout. In the absence of relaxation, and neglecting t_d, a RE-magnetometer interrogated at complete echo cycles $t = n(2\vartheta/\Omega)$ yields $\eta_{RE} = \frac{1}{\gamma_e\sqrt{t}}\frac{\vartheta}{2\sin^2(\vartheta/2)}$. As shown in Fig. 1b, RE magnetometry has thus sensitivities comparable to Ramsey spectroscopy, $\eta_{Ram} \approx 1/(\gamma_e\sqrt{t})$. Conversely, Rabi-beat magnetometry has $\eta_{Rabi} \approx \frac{\sqrt{2\Omega}}{\gamma_e}$ at large times (Supplementary Methods), which makes it unsuitable for magnetometry despite long coherence times.

To establish the sensitivity limits of RE magnetometry and compare them with other DC-magnetometry strategies, we carried out proof-of-principle experiments in single NV centres in a bulk electronic-grade diamond sample. A static magnetic field $B_{||} \approx 100\,\mathrm{G}$ effectively singles out a qubit $\{|0\rangle, |1\rangle\}$ from the NV ground-state spin triplet, as the Zeeman shift lifts the degeneracy between the $|\pm 1\rangle$ levels. The qubit is coupled to the spin-1 ^{14}N nucleus that composes the defect by an isotropic hyperfine interaction of strength $A \approx 2\pi \times 2.17\,\mathrm{MHz}$. After optical polarization into state $|0\rangle$, we apply a stream of n RE cycles using microwaves with frequency ω close to the qubit resonance $\omega_0 = \Delta + \gamma_e B_{||}$, where $\Delta = 2.87\,\mathrm{GHz}$ is the NV zero-field splitting. Because of the hyperfine coupling, ω_0 is the resonance frequency only when the nuclear state is $m_I = 0$. At room temperature, the nitrogen nucleus is unpolarized and, while its state does not change over one experimental run, in the course of the $N \sim 10^6$ experimental realizations, $\approx 2/3$ of the times the qubit is off-resonantly driven by $|\delta\omega| = A$. A typical n-cycle RE fluorescence signal is plotted in Fig. 1c for $\vartheta = \pi$ and $\Omega \approx 2\pi \times 17\,\mathrm{MHz}$, while to determine the frequency content of the signal we plot the periodogram (Supplementary Methods) in Fig. 2.

The number of distinguishable frequencies increases with interrogation time at the expense of signal-to-noise ratio. RE magnetometry not only discriminates the frequency shifts due to the hyperfine interaction (we find $A \approx 2\pi \times (2.14 \pm 0.03)$ MHz but, for interrogation times as short as 5 μs, it also reveals a small residual detuning $b \approx 2\pi \times (0.17 \pm 0.02)$ MHz from the presumed resonance. In contrast, under the same experimental conditions, Rabi magnetometry does not discern such a detuning before an interrogation time $\approx 188\,\mu\mathrm{s}$ (Supplementary Methods, and Supplementary Fig. S1). With longer interrogation times $\sim 15\,\mu\mathrm{s}$ as in Fig. 2b (also in Supplementary Fig. S2), RE can detect a frequency as small as $b \approx 2\pi \times (64 \pm 12)$ kHz.

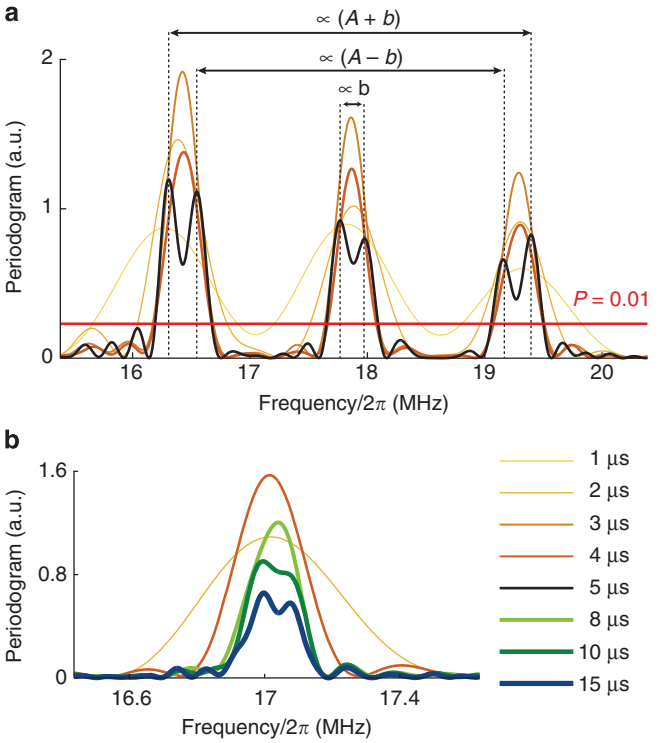

Figure 2 | The periodogram identifies the frequency content of the signal. (**a**) Experimental periodogram for π-RE sequence for increasing interrogation times (thicker lines from 1 to 5 μs, in intervals of 1 μs). The periodogram is defined as the squared magnitude of the Fourier transform of the time signal. A pair of symmetric peaks about the Rabi frequency Ω signals the existence of one detuning $\delta\omega$. The number of resolved frequencies increases with time, at the expense of signal-to-noise ratio. After 5 μs of interrogation, we can estimate both the hyperfine interaction $A \approx 2\pi \times (2.14 \pm 0.03)$ MHz and a small residual detuning from the presumed resonance, $b \approx 2\pi \times (0.17 \pm 0.02)$ MHz. In this estimate, we correct for the real rotation angle $\vartheta \approx 0.96\pi$ using the difference between the nominal and experimentally realized Rabi frequency (symmetry point in the spectrum). The uncertainty in the measurement is estimated taking into account the total interrogation time, the number of points in the time-domain signal, and the S/N (Supplementary Methods). Periodogram peaks can be tested for their statistical significance[33] (also Supplementary Methods); we confirm that all six frequency peaks are considerably more significant than a $P = 0.01$ significance level (red). (**b**) Innermost pair of frequency peaks arising from a $b \approx 2\pi \times (64 \pm 12)$ kHz residual detuning in another experimental realization, for an interrogation time of 15 μs.

To determine the experimental sensitivities, we estimate $\left|\frac{\partial\mathcal{S}}{\partial\delta\omega}\right|$ by driving the qubit with varying ω, at fixed interrogation times t (Fig. 3a). For each t, in Fig. 3b we plot the minimum $\frac{1}{\gamma_e}\frac{\Delta\mathcal{S}}{\left|\frac{\partial\mathcal{S}}{\partial\delta\omega}\right|}\sqrt{Nt}$ and compare it with the adjusted theoretical sensitivity $\eta/(C \times C_A)$. Here, $(C \times C_A) \approx (5.9 \pm 1.4) \times 10^{-3}$ in our setup, is a factor taking into account readout inefficiencies and a correction for the presence of the hyperfine interaction[1] (see also Supplementary Methods). The sensitivities agree with the theoretical model, with optimal $\sim 10\,\mu\mathrm{T Hz}^{-1/2}$, which is within the range of sensitivities achieved with other magnetometry schemes alternative to Ramsey[23,24], and with the added flexibility made possible by a suitable choice of RE rotation angle. Improved sensitivities are expected from isotopically purified diamond[25]; an adequate choice of interrogation times or polarization of the nuclear spin can easily set $C_A = 1$, while C can be improved by efficient photon collection[26] or using repeated readout methods[27].

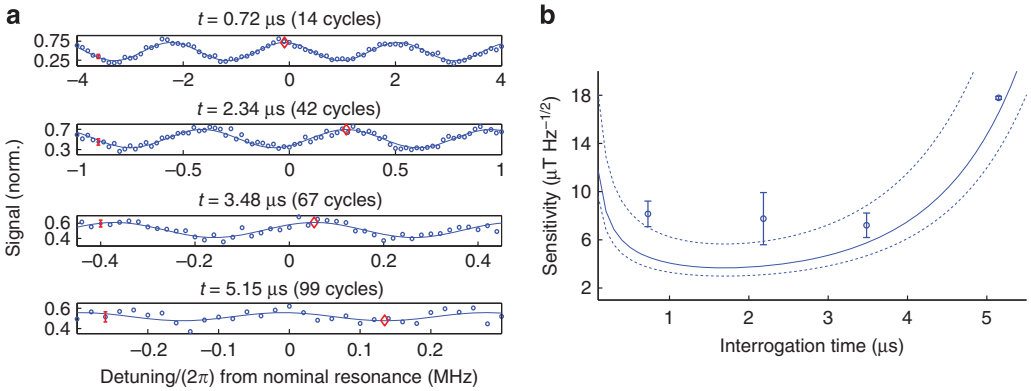

Figure 3 | Experimental sensitivity of RE magnetometry. (**a**) RE signals at fixed interrogation times, indicated on top of each sub panel, as a function of the detuning $\delta\omega$ from resonance. The signals are used to numerically calculate $\left|\frac{\partial S}{\partial \delta\omega}\right|$ and thus obtain the sensitivity η, given by equation (4). With increasing interrogation times, the slopes initially increase, indicating an improvement in η; the effect of decoherence for the longer interrogation times degrades the sensitivity, and the slopes smoothen accordingly. The different amplitude modulations are due to the three frequencies in the signal, $\{b, A \pm b\}$; polarizing the nuclear spin[34] would eliminate this modulation. From the fitted resonances for each curve (red diamonds), we estimate the true resonance to be at 0.09 ± 0.15 MHz from the presumed resonance. Typical s.d. in the measurement are indicated (red error bars). Interrogation times are chosen to coincide with minima of the sensitivity in the presence of the hyperfine interaction; in other words, the correction factor C_A is at a local maximum at those times (Supplementary Methods, and Supplementary Fig. S3). (**b**) For each fixed interrogation time, we plot the minimum sensitivity η within one oscillation period of the fitted oscillation frequency obtained in (**a**), $\tau = 2t\ \sin(\vartheta/2)/\vartheta$ (Supplementary Methods, and Supplementary Fig. S4a). The experimental points agree in trend with the theoretically expected sensitivities $\eta/(C \times C_A)$ (solid curves), here corrected for the presence of static bath noise, $\eta \rightarrow \eta e^{(t/T'_{\mathrm{RE}})^2}$. T'_{RE} was computed using a $T_2^* \approx 2.19 \pm 0.15\,\mu$s fitting from a Ramsey decay experiment (Supplementary Fig. S4b). The dashed blue lines indicate the lower (higher) bounds for the sensitivity estimated by dividing the theoretical sensitivity by the maximum (minimum) $C \times C_A$ value in the set of points. The s.d. is shown in the error bar for each point.

Effect of noise. The sensitivity of a NV magnetometer is ultimately limited by the interaction of the quantum probe with the nuclear spin bath. We model the effect of the spin bath by a classical noise source along σ_z (ref. 28), described by an Ornstein–Uhlenbeck (OU) process of strength σ and correlation time τ_c. In the limit of long τ_c (static bath), the dephasing time associated with RE (Ramsey) magnetometry is $T'_{\mathrm{RE}} = \frac{\vartheta}{\sigma\sqrt{2}\,|\sin(\vartheta/2)|}$ ($T_2^\star = T'_{\mathrm{Ram}} = \frac{\sqrt{2}}{\sigma}$) respectively (for the general case, see Supplementary Methods, and Supplementary Fig. S5a). Although at the optimum interrogation time $T'/2$ one has $\eta_{\mathrm{RE}}/\eta_{\mathrm{Ram}} = \sqrt{\frac{\vartheta}{2\sin(\vartheta/2)^3}} > 1$, RE magnetometry allows a greater flexibility in choosing the effective coherence time, as larger ϑ increase the resilience to bath noise. Thus, one can match the RE interrogation time to the duration of the field one wants to measure.

In addition, RE can yield an overall advantage when taking into consideration the dead-time t_d. If $t_d \gg T'_{\mathrm{Ram}}$, as in repeated readout methods[27], a gain in sensitivity can be reached by exploiting the longer interrogation times enabled by RE magnetometry (Supplementary Methods, and Supplementary Fig. S6). An even larger advantage is given by AC magnetometry with $2\pi k$-RE[20], as RE provides better protection than pulsed DD schemes[17,20].

Excitation field instabilities along σ_x also accelerate the decay of RE and Rabi signals. However, provided the echo period is shorter than τ_c, RE magnetometry corrects for stochastic noise in Rabi frequency (Supplementary Methods, and Supplementary Fig. S5b). This protection was demonstrated experimentally by applying static and OU noise ($\tau_c \approx 200$ ns) in the excitation microwave, both with strength $0.05\,\Omega$. The results for Rabi and $\vartheta = \{\pi, 5\pi\}$-RE sequences in Fig. 4 clearly show that whereas the Rabi signal decays within $\approx 0.5\,\mu$s, 5π-RE refocuses static excitation noise and presents only a very weak decay under finite-correlation noise after much longer interrogation times $\approx 3\,\mu$s, in agreement with the theoretical prediction; π-RE is robust against the same noise profiles.

Discussion

The unique ability of the RE-magnetometer to adjust its response to distinct noise sources is relevant when the sample producing the magnetic field of interest is immersed in a realistic environment; moreover, the field source might itself have a finite duration or duty cycle. Most experimentally relevant fields, such as those arising from biological samples, might last only for a finite amount of time, when triggered, or be slowly varying so that one can only record their time-average. Thus, it becomes interesting to be able to tune the interrogation time in order to capture and average over the complete physical process. The advantage is two-fold: the protection from noise can be tuned by changing the echo angle, thus allowing the interrogation times to be varied. Techniques for repeated readout in the presence of a strong magnetic field $\gtrsim 1{,}000$ G (ref. 27) (also Supplementary Methods) can at once improve sensitivities and enable the use of much lower qubit resonance frequencies $\sim$MHz, preferable in biological settings.

Additionally, a RE-magnetometer can discriminate magnetic noise sources given the sensor's well-understood decoherence behaviour under different noise profiles, effectively enabling noise spectroscopy for both σ_z and σ_x-type noises.

NV centre-based RE magnetometry could find useful application, for example, to sense the activity of differently-sized calcium signalling domains in living cells, more specifically in neurons. Transient calcium fluxes regulate a myriad of cell reactions[29]. The signalling specificity of such fluxes is determined by their duration and mean travelled distance between membrane channel and cytoplasm receptor. The smaller, faster-signalling domains have resisted thorough investigation via both diffraction-limited optical microscopy[29], and the use of fluorescing dyes, which do not respond fast or accurately enough to Ca^{2+} transients[30]. The magnetic field produced by as few as 10^5 Ca^{2+}, being diffused within $\sim 10\,\mu$s through a $\sim$200-nm domain, can be picked up by a nanodiamond scanning

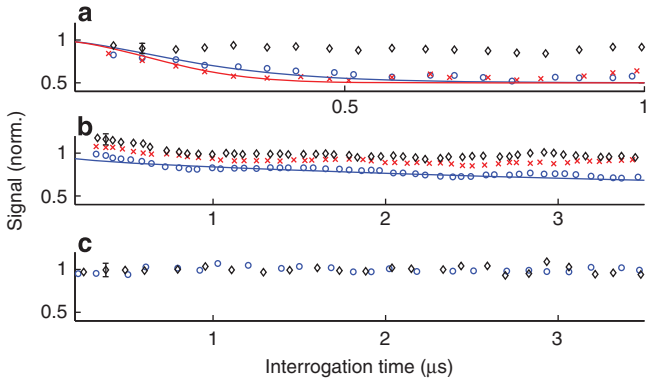

Figure 4 | The RE is robust against added microwave frequency noise. Forty realizations of both static (red) and Ornstein–Uhlenbeck (OU, $\tau_c = 200$ ns, blue) microwave noise of strength $0.05\,\Omega$, where $\Omega \approx 2\pi \times 19$ MHz is the Rabi frequency, for (**a**) Rabi, (**b**) 5π-RE and (**c**) π-RE sequences. We note that the correlation time of the driving field noise was purposely set much shorter than what usually observed in experiments in order to enhance the different behaviour of π-RE and 5π-RE. Typical s.d. in the measurement are indicated (black error bars). (**a**) We plot the peak of the Rabi fringes in the presence of static (red crosses) and OU (blue circles) microwave noise, which are in agreement with the expected theoretical decay (solid blue line and solid red line, respectively) (Supplementary Methods and Supplementary Fig. 5b). The oscillations at the tail of the signals are due to the finite number of experimental realizations. The peaks of a no-noise Rabi experiment are plotted for comparison (black diamonds). (**b**) The peak of the 5π-RE revivals are plotted in the presence of static (red crosses) and OU (blue circles) microwave noise; the peaks of the 5π-RE in the absence of microwave noise are also plotted for comparison (black diamonds). Although the echo virtually does not decay in the presence of static noise, under the effect of stochastic noise, the echo decays only weakly as stipulated by theory (solid blue line) (Supplementary Methods and Supplementary Fig. 5b). (**c**) The peak of the π-RE revivals are plotted in the presence of OU microwave noise (blue circles); virtually no decay is found if compared with the peaks of a no-noise experiment (black diamonds).

sensor[31,32] with sensitivity $\sim 10\,\mu\mathrm{THz}^{-1/2}$ placed at close proximity ~ 10 nm (Supplementary Methods). The trade-off between sensitivity and optimal interrogation time under RE magnetometry can be optimized to the characteristics of the signalling domain under study by a suitable choice of ϑ.

In conclusion, we have demonstrated a quantum magnetometry scheme based on composite pulses. Its key interest stems both from the continuous-excitation character, offering superior performance for solid state sensors such as the NV centre, and from the possibility of tuning the sensor's coherence time and sensitivity in the presence of variable or unknown sensing environments, to protect from or map noise sources. Current technology enables immediate implementation of such scheme at the nanoscale.

Methods

Quantum magnetometer description. The NV centre is a naturally occurring point defect in diamond, composed of a vacancy adjacent to a substitutional nitrogen in the carbon lattice. The ground state of the negatively charged NV centre is a spin triplet with zero-field splitting $\Delta = 2.87$ GHz between the $m_S = 0$ and $m_S = \pm 1$ sub-levels. Coherent optical excitation at 532 nm promotes the quantum state of the defect non-resonantly to the first orbital excited state. Although the $m_S = 0$ state mostly relaxes with phonon-mediated fluorescent emission ($\approx$650–800 nm), the $m_S = \pm 1$ states have in addition an alternative, non-radiative decay mode to the $m_S = 0$ state via metastable singlet states. Owing to this property, each ground state is distinguishable by monitoring the intensity of emitted photons during a short pulse of optical excitation. Additionally, continuous optical excitation polarizes the NV into the $m_S = 0$ state. We apply a magnetic field (≈ 100 G) along a crystal axis $\langle 111 \rangle$ to lift the degeneracy between the $m_S = \pm 1$ states and drive an effective two-level system $m_S = \{0,1\}$ at the resonant frequency ($\omega_0 \approx 3.15$ GHz) obtained by continuous wave electron spin resonance and Ramsey fringe experiments.

Experimental setup description. Experiments were run at room-temperature with single NV centres from an electronic-grade single crystal plate ([100] orientation, Element 6) with a substitutional nitrogen concentration <5 ppb. The fluorescence of single NV centres is identified by a home-built confocal scanning microscope. The sample is mounted on a piezo stage (Nano-3D200, Mad City Labs). The excitation at 532 nm is provided by a diode-pumped laser (Coherent Compass 315M), and fluorescence in the phonon sideband ($\sim$650–800 nm) is collected by a X100, NA = 1.3 oil immersion objective (Nikon Plan Fluor). The fluorescence photons are collected into a single-mode broadband fibre of NA = 0.12 (Font Canada) and sent to a single-photon counting module (SPCM-AQRH-13-FC, Perkin Elmer) with acquisition time 100 or 200 ns.

Laser pulses for polarization and detection are generated by an acousto-optic modulator with rise time $\lesssim 7$ ns (1250C-848, Isomet). A signal generator (N5183A-520, Agilent) provides microwave fields to coherently manipulate the qubit. An arbitrary waveform generator at 1.2 GS/s (AWG5014B, Tektronix) is employed to shape microwave pulses with the help of an I/Q mixer (IQ-0318L, Marki Microwave), and to time the whole experimental sequence. Microwaves are amplified (GT-1000A, Gigatronics) and subsequently delivered to the sample by a copper microstrip mounted on a printed circuit board, fabricated in MACOR to reduce losses.

A static magnetic field is applied by a permanent magnet (BX0X0X0-N52, K&J Magnetics) mounted on a rotation stage, which in turn is attached to a three-axis translation stage; this arrangement enables the adjustment of the magnetic field angle with respect to the sample. The magnetic field is aligned along a [111] axis by maximizing the Zeeman splitting in a CW ESR spectrum.

In each experimental run, we normalize the signal with respect to the reference counts from the $m_S = \{0,1\}$ states, where the transfer to state $m_S = 1$ is done by adiabatic passage.

References

1. Taylor, J. M. *et al.* High-sensitivity diamond magnetometer with nanoscale resolution. *Nat. Phys.* **4,** 810–816 (2008).
2. Maze, J. R. *et al.* Nanoscale magnetic sensing with an individual electronic spin qubit in diamond. *Nature* **455,** 644–647 (2008).
3. Balasubramanian, G. *et al.* Magnetic resonance imaging and scanning probe magnetometry with single spins under ambient conditions. *Nature* **445,** 648–651 (2008).
4. Jarmola, A., Acosta, V. M., Jensen, K., Chemerisov, S. & Budker, D. Temperature- and magnetic-field-dependent longitudinal spin relaxation in nitrogen-vacancy ensembles in diamond. *Phys. Rev. Lett.* **108,** 197601 (2012).
5. Waldherr, G. *et al.* High-dynamic-range magnetometry with a single nuclear spin in diamond. *Nat. Nanotech.* **7,** 105–108 (2012).
6. Childress, L. *et al.* Coherent dynamics of coupled electron and nuclear spin qubits in diamond. *Science* **314,** 281–285 (2006).
7. Cappellaro, P. *et al.* Environment-assisted metrology with spin qubits. *Phys. Rev. A* **85,** 032336 (2012).
8. Goldstein, G. *et al.* Environment-assisted precision measurement. *Phys. Rev. Lett.* **106,** 140502 (2011).
9. McGuinness, L. P. *et al.* Quantum measurement and orientation tracking of fluorescent nanodiamonds inside living cells. *Nat. Nanotech.* **6,** 358–363 (2011).
10. Ramsey, N. F. *Molecular Beams* (Oxford University, 1990).
11. Hahn, E. L. Spin echoes. *Phys. Rev.* **80,** 580–594 (1950).
12. Meiboom, S. & Gill, D. Modified spin-echo method for measuring nuclear relaxation times. *Rev. Sc. Instr.* **29,** 688 (1958).
13. Kosugi, N., Matsuo, S., Konno, K. & Hatakenaka, N. Theory of damped Rabi oscillations. *Phys. Rev. B* **72,** 172509 (2005).
14. Fedder, H. *et al.* Towards T_1-limited magnetic resonance imaging using Rabi beats. *Appl. Phys. B* **102,** 497–502 (2011).
15. Levitt, M. H. Composite pulses. *Prog. Nucl. Mag. Res. Spect.* **18,** 61–122 (1986).
16. Solomon, I. Multiple echoes in solids. *Phys. Rev.* **110,** 61–65 (1958).
17. Laraoui, A. & Meriles, C. A. Rotating frame spin dynamics of a nitrogen-vacancy center in a diamond nanocrystal. *Phys. Rev. B* **84,** 161403 (2011).
18. Cai, J. -M. *et al.* Robust dynamical decoupling with concatenated continuous driving. *New J. Phys.* **14,** 113023 (2012).
19. Xu, X. *et al.* Coherence-protected quantum gate by continuous dynamical decoupling in diamond. *Phys. Rev. Lett.* **109,** 070502 (2012).
20. Hirose, M., Aiello, C. D. & Cappellaro, P. Continuous dynamical decoupling magnetometry. *Phys. Rev. A.* **86,** 062320 (2012).
21. Haeberlen, U. *High Resolution NMR in Solids: Selective Averaging* (Academic Press, 1976).

22. Wineland, D. J., Bollinger, J. J., Itano, W. M., Moore, F. L. & Heinzen, D. J. Spin squeezing and reduced quantum noise in spectroscopy. *Phys. Rev. A* **46,** R6797 (1992).
23. Schoenfeld, R. S. & Harneit, W. Real-time magnetic field sensing and imaging using a single spin in diamond. *Phys. Rev. Lett.* **106,** 030802 (2011).
24. Dréau, A. *et al.* Avoiding power broadening in optically detected magnetic resonance of single NV defects for enhanced DC magnetic field sensitivity. *Phys. Rev. B* **84,** 195204 (2011).
25. Balasubramanian, G. *et al.* Ultralong spin coherence time in isotopically engineered diamond. *Nat. Mater.* **8,** 383–387 (2009).
26. Babinec, T. M. *et al.* A diamond nanowire single-photon source. *Nat. Nanotech.* **5,** 195–199 (2010).
27. Neumann, P. *et al.* Single-shot readout of a single nuclear spin. *Science* **5991,** 542–544 (2010).
28. Klauder, J. R. & Anderson, P. W. Spectral diffusion decay in spin resonance experiments. *Phys. Rev.* **125,** 912–932 (1962).
29. Augustine, G. J., Santamaria, F. & Tanaka, K. Local calcium signaling in neurons. *Neuron* **40,** 331–346 (2003).
30. Keller, D. X., Franks, K. M., Bartol, Jr T. M. & Sejnowski, T. J. Calmodulin activation by calcium transients in the postsynaptic density of dendritic spines. *PLoS ONE* **3,** e2045 (2008).
31. Degen, C. L. Scanning magnetic field microscope with a diamond single-spin sensor. *Appl. Phys. Lett.* **92,** 243111 (2008).
32. Grinolds, M. S., Maletinsky, P., Hong, S., Lukin, M. D., Walsworth, R. L. & Yacoby, A. Quantum control of proximal spins using nanoscale magnetic resonance imaging. *Nat. Phys.* **7,** 687–692 (2011).
33. Wei, W. W. S. *Time Series Analysis: Univariate and Multivariate Methods* (Pearson Addison Wesley, 2006).
34. Jacques, V. *et al.* Dynamic polarization of single nuclear spins by optical pumping of nitrogen-vacancy color centers in diamond at room temperature. *Phys. Rev. Lett.* **102,** 057403 (2009).

Acknowledgements

C.D.A. thanks Boerge Hemmerling, Michael G. Schmidt and Marcos Coque Jr. for stimulating discussions. This work was supported in part by the US Army Research Office through a MURI grant No. W911NF-11-1-0400 and by DARPA (QuASAR programme). C.D.A. acknowledges support from the Schlumberger Foundation.

Author contributions

C.D.A., M.H. and P.C. conceived the experiment and performed the theoretical analysis. C.D.A. and M.H. carried out the measurements and analysis of the data. All authors discussed the results and contributed to the manuscript.

Additional information

Supplementary Information accompanies this paper at http://www.nature.com/naturecommunications

Competing financial interests: The authors declare no competing financial interests.

Reprints and permission information is available online at http://npg.nature.com/reprintsandpermissions/

How to cite this article: Aiello, C. D. *et al.* Composite-pulse magnetometry with a solid-state quantum sensor. *Nat. Commun.* 4:1419 doi: 10.1038/ncomms2375 (2013).

Supplementary Information to "Composite-pulse magnetometry with a solid-state quantum sensor"

Clarice D. Aiello, Masashi Hirose, and Paola Cappellaro*
Department of Nuclear Science and Engineering,
Massachusetts Institute of Technology, Cambridge, MA 02139, USA

SUPPLEMENTARY FIGURES

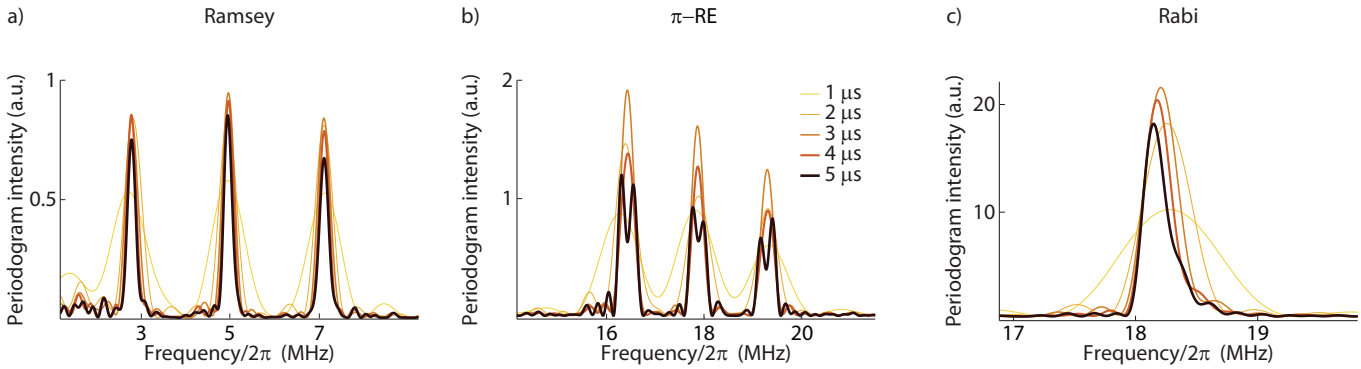

SUPPLEMENTARY FIG. S1. **Experimental periodograms for increasing interrogation times up to** 5μ**s.** a) Ramsey (5MHz detuned from the presumed resonance), b) π-rotary-echo and c) Rabi sequences. There is a trade-off between signal intensity and sensitivity to the detunings $\{b, A \pm b\}$ in the signal.

* pcappell@mit.edu

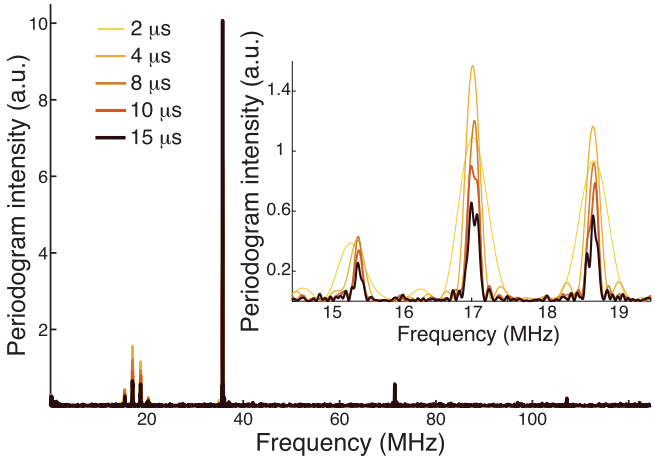

SUPPLEMENTARY FIG. S2. **Rotary-echo periodogram over the full spectrum.** Frequencies corresponding to the even harmonics of the Rabi frequency Ω, which are present in the signal, but which are not contemplated by the first order of average Hamiltonian theory, can be clearly identified. In the inset, the signal peaks arising from the frequencies of interest are shown for interrogation times much longer than the dephasing time T'_{RE}.

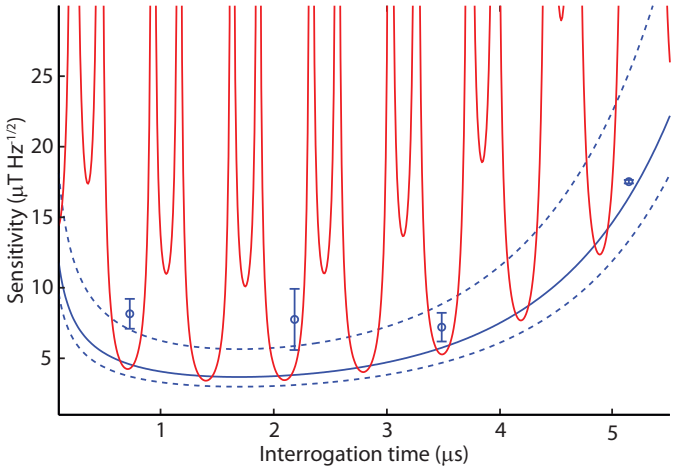

SUPPLEMENTARY FIG. S3. **Experimental sensitivity taking into account the time dependence of $\overline{C_A(t)}$.** This plot superimposes to Fig. 3 in the main text the expected sensitivity of the quantum magnetometer for all times of the correction factor $\overline{C \times C_A(t)}$ (solid red line). The experimental points (blue circles) are chosen accordingly, so as to have each one of the four realizations of C_A at a local maximum. We see that the data do indeed correspond to points of maximal sensitivity of the quantum magnetometer. We note that the solid blue curve is estimated using an averaged correction factor $\overline{C \times C_A}$, for the four experimental realizations of C and C_A.

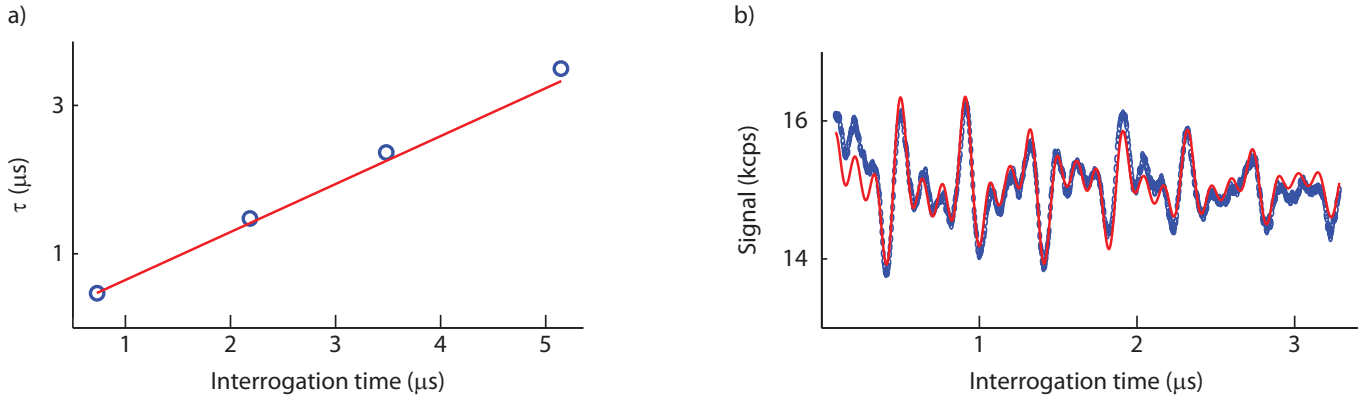

SUPPLEMENTARY FIG. S4. **Fitted parameters used to determine the experimental sensitivity.** a) The fitted periods τ (blue dots) are linear in the interrogation time t and agree well with the theoretically expected time $2t\sin(\vartheta/2)/\vartheta$ (red line). b) The Ramsey signal (blue circles) is fitted to $\mathcal{S}_{\rm Ram} = k_1 - k_2\left[\cos(\delta\omega t) + \cos((A+\delta\omega)t) + \cos((A-\delta\omega)t)\right] e^{-(t/T_2^\star)^2}$ (red), with fitting parameters $\{k_1, k_2, \delta\omega, A, T_2^\star\}$. In particular, $T_2^\star \sim 2.19 \pm 0.15\mu$s.

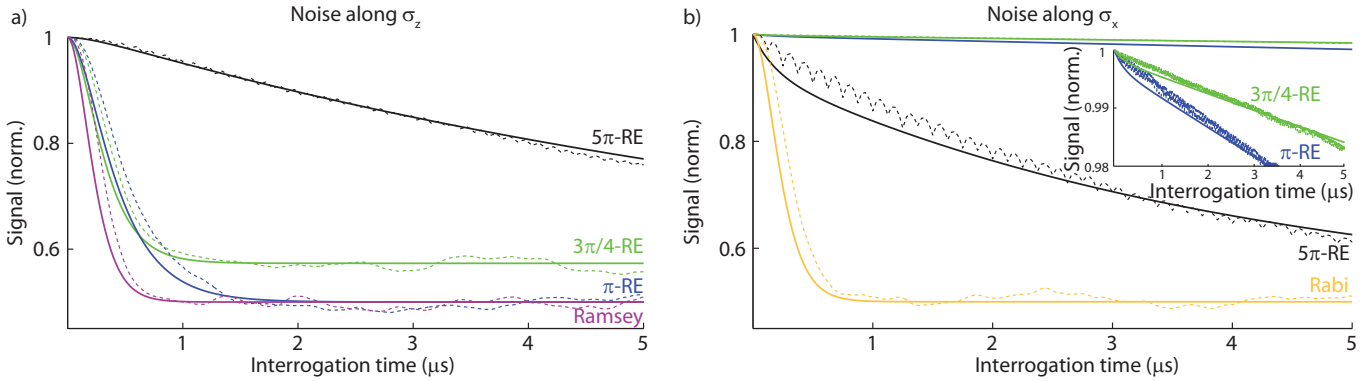

SUPPLEMENTARY FIG. S5. **Simulated signal decay in the presence of stochastic noise**. a) In the presence of stochastic bath noise, different ϑ-RE with $\vartheta = \{3\pi/4, \pi, 5\pi\}$ (green, blue, black) are compared against a Ramsey sequence (purple); numerical simulations (dashed lines) agree with the formulas presented in the text (solid lines). The Ramsey sequence is the least resilient to bath noise, whereas one can adjust the dephasing of the RE by the choice of ϑ; RE sequences are more resilient to bath noise with correlation times shorter than the echo period. The used numerical parameters are: $\Omega = 2\pi\times$20MHz, $\delta\omega = 2\pi\times$2MHz, $\tau_c = 200$ns, $\sigma = 0.05\Omega$. b) In the presence of stochastic noise in the excitation field, the situation is inverted: RE sequences refocus microwave noise with correlation times longer than the echo period; the decay of the Rabi sequence (orange) is plotted for comparison. Used parameters are the same as in a), except for $\delta\omega = 0$.

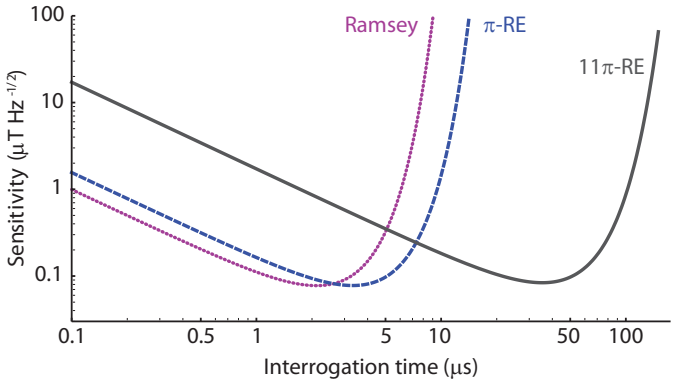

SUPPLEMENTARY FIG. S6. **Sensitivity with repeated readouts.** We compare the achievable sensitivity for Ramsey (purple, dotted) and rotary-echo (π-RE, blue, dashed; 11π-RE, gray) sequences, when using the repeated readout scheme, with $N_{\rm r} = 100$ and the time per each readout $t_{\rm r} = 1.5\mu$s. In the presence of dephasing with $T_2^\star = 3\mu$s, the longer angle RE achieves good sensitivity for much longer interrogation times.

SUPPLEMENTARY METHODS

Dynamics under rotary-echo sequence

Consider a two-level system, $|0\rangle$ and $|1\rangle$, with resonance frequency ω_0. The qubit is excited by radiation of frequency ω with associated Rabi frequency Ω and phase modulation $\varphi(t)$, such that the magnetic field amplitude is $\Omega\cos(\omega t+\varphi(t))$. The Hamiltonian is then

$$\mathcal{H}_{\rm lab}=\begin{pmatrix} 0 & \Omega\cos(\omega t+\varphi(t)) \\ \Omega\cos(\omega t+\varphi(t)) & \omega_0 \end{pmatrix} . \tag{S1}$$

In a frame rotating with the excitation field, the operator

$$U_{\rm rot}=\begin{pmatrix} 1 & 0 \\ 0 & e^{i\omega t} \end{pmatrix} \tag{S2}$$

transforms the Hamiltonian to

$$\mathcal{H}=\begin{pmatrix} 0 & \Omega\cos(\omega t+\varphi(t))e^{-i\omega t} \\ \Omega\cos(\omega t+\varphi(t))e^{i\omega t} & \omega_0-\omega \end{pmatrix} . \tag{S3}$$

Applying the rotating wave approximation and setting set $\delta\omega\equiv\omega_0-\omega$, the Hamiltonian reads

$$\mathcal{H}\approx\begin{pmatrix} 0 & \frac{\Omega}{2}e^{i\varphi(t)} \\ \frac{\Omega}{2}e^{-i\varphi(t)} & \delta\omega \end{pmatrix} . \tag{S4}$$

One rotary-echo (RE) is composed of two identical pulses of nominal rotation angle ϑ applied with excitation phases shifted by π. Under a sequence of RE, $e^{i\varphi(t)}=\mathbb{SW}(t)$, with $\mathbb{SW}(t)$ the square wave of period $T=\frac{2\vartheta}{\Omega}$ equal to the RE cycle time:

$$\mathbb{SW}(t)=\frac{4}{\pi}\sum_{k=1,\rm odd}^{\infty}\frac{1}{k}\sin\left(\frac{k\pi\Omega t}{\vartheta}\right) . \tag{S5}$$

On resonance ($\delta\omega=0$) the evolution operator is trivially obtained:

$$U_0=\begin{pmatrix} \cos(\frac{\Omega}{2}\mathbb{TW}(t)) & -i\sin(\frac{\Omega}{2}\mathbb{TW}(t)) \\ -i\sin(\frac{\Omega}{2}\mathbb{TW}(t)) & \cos(\frac{\Omega}{2}\mathbb{TW}(t)) \end{pmatrix}=\cos\left(\frac{\Omega}{2}\mathbb{TW}(t)\right)\mathbb{1}-i\sin\left(\frac{\Omega}{2}\mathbb{TW}(t)\right)\sigma_x , \tag{S6}$$

where $\mathbb{TW}(t)$ is the triangular wave representing the integral of $\mathbb{SW}(t)$,

$$\mathbb{TW}(t)=\frac{\vartheta}{2\Omega}-\frac{4\vartheta}{\pi^2\Omega}\sum_{k=1,\rm odd}^{\infty}\frac{1}{k^2}\cos\left(\frac{k\pi\Omega t}{\vartheta}\right) . \tag{S7}$$

Using U_0 we make a transformation to the toggling frame of the microwave [35] to obtain the Hamiltonian $\tilde{\mathcal{H}}$:

$$\tilde{\mathcal{H}}=\frac{\delta\omega}{2}\begin{pmatrix} 1-\cos(\Omega\mathbb{TW}(t)) & i\sin(\Omega\mathbb{TW}(t)) \\ -i\sin(\Omega\mathbb{TW}(t)) & 1+\cos(\Omega\mathbb{TW}(t)) \end{pmatrix}=\frac{\delta\omega}{2}\left[\mathbb{1}-\cos(\Omega\mathbb{TW}(t))\sigma_z-\sin(\Omega\mathbb{TW}(t))\sigma_y\right] . \tag{S8}$$

$\tilde{\mathcal{H}}$ is periodic with T and has a strength $T\delta\omega\ll 1$, and can thus be analyzed with an average Hamiltonian expansion. In order to do so, we first express the elements of $\tilde{\mathcal{H}}$ in their Fourier series:

$$\cos(\Omega\mathbb{TW}(t))=\frac{\sin\vartheta}{\vartheta}+2\vartheta\sin\vartheta\sum_{k=1,\rm odd}^{\infty}\frac{(-1)^k}{\vartheta^2-k^2\pi^2}\cos\left(\frac{k\pi\Omega t}{\vartheta}\right) ; \tag{S9}$$

$$\sin(\Omega\mathbb{TW}(t)) = \frac{1-\cos\vartheta}{\vartheta} + 2\vartheta \sum_{k=1,\text{odd}}^{\infty} \frac{(-1)^k((-1)^k - \cos\vartheta)}{\vartheta^2 - k^2\pi^2} \cos\left(\frac{k\pi\Omega t}{\vartheta}\right) . \tag{S10}$$

To first order then,

$$\overline{\mathcal{H}}^{(1)} = \frac{1}{T}\int_0^T \tilde{\mathcal{H}}(t')\mathrm{d}t' = \frac{\delta\omega}{\vartheta}\sin\left(\frac{\vartheta}{2}\right)\begin{pmatrix} -\cos(\vartheta/2) & i\sin(\vartheta/2) \\ -i\sin(\vartheta/2) & \cos(\vartheta/2) \end{pmatrix} = -\frac{\delta\omega}{\vartheta}\sin\left(\frac{\vartheta}{2}\right)\left[\cos\left(\frac{\vartheta}{2}\right)\sigma_z - \sin\left(\frac{\vartheta}{2}\right)\sigma_y\right]. \tag{S11}$$

For n rotary cycles, the propagator is approximated by $U_{\text{RE}} = e^{i\tilde{\mathcal{H}}(t)t} \approx e^{inT\overline{\mathcal{H}}^{(1)}}$. The population of a system initially prepared in $|0\rangle$, under the action of U_{RE}, is described at full echo times by the signal

$$\mathcal{S}(n) \approx \frac{1}{2}\left[1 + \cos^2\left(\frac{\vartheta}{2}\right) + \sin^2\left(\frac{\vartheta}{2}\right)\cos\left(\frac{4\delta\omega n}{\Omega}\sin\left(\frac{\vartheta}{2}\right)\right)\right] . \tag{S12}$$

Extending the above approximation to include the fast Rabi-like oscillations of frequency $\frac{\pi\Omega}{(\vartheta \bmod 2\pi)}$, we obtain

$$\mathcal{S}(t) \approx \frac{1}{2}\left[1 + \cos^2\left(\frac{\vartheta}{2}\right) + \sin^2\left(\frac{\vartheta}{2}\right)\cos\left(\frac{2\delta\omega t}{\vartheta}\sin\left(\frac{\vartheta}{2}\right)\right)\cos\left(\frac{\pi\Omega t}{(\vartheta \bmod 2\pi)}\right)\right] , \tag{S13}$$

indicating the presence of two spectral lines at $\frac{\pi\Omega}{(\vartheta \bmod 2\pi)} \pm \frac{2\delta\omega}{\vartheta}\sin\left(\frac{\vartheta}{2}\right)$ for each existing detuning $\delta\omega$.

Our numerical studies suggest the existence of further signal components arising from higher frequency components in the Fourier expansion, which are not contemplated by the first-order approximation outlined above. Such components are $\propto \cos\left(\frac{2\delta\omega t}{\vartheta}\sin\left(\frac{\vartheta}{2}\right)\right)\cos\left(\frac{(2k+1)\pi\Omega t}{(\vartheta \bmod 2\pi)}\right)$ and $\propto \cos\left(\frac{2k\pi\Omega t}{(\vartheta \bmod 2\pi)}\right)$, $k \in \mathbb{Z}$, thus being linked to split pairs of spectral lines around $\frac{(2k+1)\pi\Omega t}{(\vartheta \bmod 2\pi)}$, and single lines at $\frac{2k\pi\Omega t}{(\vartheta \bmod 2\pi)}$.

Rabi-beat magnetometry

Rabi-beat magnetometry using a single solid-state qubit was recently demonstrated [14]. The scheme presupposes the existence of an absolute frequency standard against which one wishes to resolve a nearby frequency. For magnetometry purposes then,

$$\mathcal{S} = \frac{1}{2}(\mathcal{S}_{\text{Rabi}}(\delta\omega) - \mathcal{S}_{\text{Rabi}}(0)) , \tag{S14}$$

where $\delta\omega$ denotes a detuning from the frequency standard. The sensitivity reads

$$\eta = \frac{1}{\gamma_{\text{e}}}\lim_{\delta\omega\to 0}\frac{\Delta\mathcal{S}}{|\frac{\partial\mathcal{S}}{\partial\delta\omega}|}\sqrt{t} \approx \frac{\sqrt{2\Omega}}{\gamma_{\text{e}}}\sqrt{\frac{t\Omega}{2 - 2\cos(t\Omega) - t\Omega\sin(t\Omega)}} ; \tag{S15}$$

η is close to minima at $t \approx (2k + \frac{3}{2})\frac{\pi}{\Omega}$, yielding

$$\eta_{\min} \approx \frac{\sqrt{2\Omega}}{\gamma_e}\Big/\sqrt{1 + \frac{2}{t\Omega}} , \tag{S16}$$

which tends to $\sqrt{2\Omega}/\gamma_{\text{e}}$ for increasingly large interrogation times.

Periodogram

The periodogram is defined as the squared magnitude of the Fourier transform (FT) of the signal $\mathcal{S}(t)$ at times t_j $(j = 1, \ldots, M)$, $\mathcal{P} \equiv \frac{1}{M}|\sum_{j=1}^{M} d_j e^{i\omega t_j}|^2$, where d_j are the M data points [36].

Unlike the FT, the periodogram does provide bounds for frequency estimation from spectral analysis, besides being able to accommodate for noise profiles beyond static and white noise [36]. Take a simple sinusoidal signal $d_t = K\cos(2\pi f t) + e_t$, where e_t is the added noise characterized by a (least informative) Gaussian probability

distribution $\mathsf{Normal}(0,\sigma^2)$, with σ in circular frequency units. To σ is assigned Jeffrey's prior $\frac{1}{\sigma}$, which indicates complete ignorance of this scale parameter. Under these conditions, the estimate frequency content of the signal is given by $f_{\rm est} = f_{\rm peak} \pm \delta f$, where $f_{\rm peak}$ is the frequency of the periodogram peak, and

$$\delta f = \frac{2\sqrt{3}}{\pi} \frac{\sigma}{Kt\sqrt{M}} \ . \tag{S17}$$

Here t is the total interrogation time for the M data points. δf correctly takes into account the effect of both the interrogation duration t and the S/N $\equiv \frac{K_{\rm RMS}}{\sigma} = \frac{K}{\sqrt{2}\sigma}$, and is shown to correspond to the classical Cramer-Rao bound [37]. Note that δf is in general smaller than the so-called Fourier limit, $\delta f_{\rm Fl} = \frac{1}{2t}$. The method is readily applicable to signals with multiple frequency content $\{f_i\}$.

In Supplementary Fig. S1, we compare typical experimental periodograms for π-RE, Ramsey and Rabi signals taken under the same conditions, for increasing interrogation times. The Ramsey periodogram, despite its lower signal intensity, clearly shows the 3 detunings $\{b + 2\pi\times 5\text{MHz}, A \pm (b + 2\pi\times 5\text{MHz})\}$ present in the signal after 1μs; π-RE is sensitive to the residual detuning $b \sim 2\pi\times 0.17$MHz as explained in the main text after 5μs; finally, the Rabi sequence would only become sensitive to b after an interrogation time $\sim 188\mu$s, which is reflected in the broad single peak of the periodogram.

We estimate the statistical significance level p of individual peaks [33]. Letting I_m be the intensity of m-th largest ordinate among the total M in the periodogram, and calculating

$$T_m = \frac{I_m}{\sum_k I_k - \sum_{l=1}^{m} I_l} \ , \tag{S18}$$

the statistical significance of the m-th peak p_m is approximated by

$$p_m \approx (M - (m-1))(1 - T_m)^{M-m} \ . \tag{S19}$$

To determine δf, we first estimate the S/N for each periodogram peak by dividing the peak area by the noise floor below the line of $p = 0.01$.

The periodogram, if plotted over the full spectrum as in Supplementary Fig. S2, exhibits very high peaks corresponding to the even harmonics of Ω which are present in the signal, but which are not taken into account by the first order of average Hamiltonian theory. In the inset, the peak structure originated from the detunings of interest is plotted for times much longer than the dephasing time $T'_{\rm RE}$.

Experimental sensitivity

For a fixed interrogation time t, and scanning the detuning from resonance $\delta\omega$, we expect to observe the signal

$$\mathcal{S}(\delta\omega) \propto \cos\left(\frac{2\delta\omega t}{\vartheta}\sin\left(\frac{\vartheta}{2}\right)\right) \equiv \cos\left(\delta\omega\tau\right) \ , \tag{S20}$$

with $\tau = \frac{2t}{\vartheta}\sin\left(\frac{\vartheta}{2}\right)$.

In every experimental run, reference curves are acquired along with the signal $\mathcal{S}$; they are noted $\mathcal{R}_0$ for the $|0\rangle$ state as obtained after laser polarization, and $\mathcal{R}_1$ for the $|1\rangle$ state as calibrated by adiabatic inversion. The signal is then normalized as

$$\overline{\mathcal{S}} = \frac{\mathcal{S} - \mathcal{R}_1}{\mathcal{R}_0 - \mathcal{R}_1} \ ; \tag{S21}$$

The standard deviation of the normalized signal is readily obtained

$$\Delta\overline{\mathcal{S}} = \sqrt{(\Delta\mathcal{R}_0)^2\left|\frac{\mathcal{S}-\mathcal{R}_1}{(\mathcal{R}_0-\mathcal{R}_1)^2}\right|^2 + (\Delta\mathcal{R}_1)^2\left|\frac{\mathcal{S}-\mathcal{R}_1}{(\mathcal{R}_0-\mathcal{R}_1)^2} - \frac{1}{\mathcal{R}_0-\mathcal{R}_1}\right|^2 + (\Delta\mathcal{S})^2\left|\frac{1}{\mathcal{R}_0-\mathcal{R}_1}\right|^2} \ . \tag{S22}$$

The sensitivity is calculated for the whole signal

$$\eta(\delta\omega) = \frac{1}{\gamma_e}\frac{\Delta\overline{\mathcal{S}}}{|\frac{\partial\overline{\mathcal{S}}}{\partial\delta\omega}|}\sqrt{Nt}\ ; \tag{S23}$$

for each fixed interrogation time t, we single out the minimum sensitivity $\eta(\delta\omega)$ within one period of the fitted oscillation period τ, depicted in Supplementary Fig. S4.a.

The standard deviation for the sensitivity measurements is obtained by

$$\Delta\eta = \frac{1}{\gamma_e}\left|\frac{\partial\eta}{\partial\overline{\mathcal{S}}}\right|\Delta\overline{\mathcal{S}}\sqrt{Nt} = \frac{1}{\gamma_e}\left|\frac{1-2\overline{\mathcal{S}}}{2\sqrt{\overline{\mathcal{S}}(1-\overline{\mathcal{S}})}}\frac{1}{\frac{\partial\overline{\mathcal{S}}}{\partial\delta\omega}}\right|\Delta\overline{\mathcal{S}}\sqrt{Nt}\ . \tag{S24}$$

Additionally, to every point in the plot there corresponds a factor C taking into account imperfect state detection [1, 38]. While the theoretical signal $\mathcal{S}$ represents the population in the $|0\rangle$ state, measured from the observable $M \equiv |0\rangle\langle 0|$, the experimental signal records photons emitted by both $|0\rangle$ and $|1\rangle$ states, so that the measurement operator is best experimentally described by $M' \equiv n_0|0\rangle\langle 0| + n_1|1\rangle\langle 1|$. Here, $\{n_0, n_1\}$ are Poisson-distributed variables that indicate the number of collected photons; if perfect state discrimination were possible, $n_0 \to \infty$ and $n_1 \to 0$. Including this effect, after n full echo cycles, the signal is modified to

$$\mathcal{S}'(n) \approx \frac{1}{4}\left[(3n_0 + n_1 + (n_0 - n_1)\cos\vartheta) + (n_0 - n_1 - (n_0 - n_1)\cos\vartheta)\cos\left(\frac{4\delta\omega n}{\Omega}\sin\left(\frac{\vartheta}{2}\right)\right)\right]\ . \tag{S25}$$

We calculate the sensitivity for $\overline{\mathcal{S}'}$ in the best-case scenario of minimum sensitivity given by the accumulated phase $\left(\frac{4\delta\omega n}{\Omega}\sin\left(\frac{\vartheta}{2}\right)\right) = \frac{\pi}{2}$, and note the existence of a factor C, with respect to the ideal sensitivity, $\eta_{M'} = \eta_M/C$:

$$C^{-1} = \sqrt{1 + \frac{1}{2} + \frac{(-11n_0 + 5n_1)}{2(n_0 - n_1)^2} + \frac{\cos\vartheta}{2}\left(1 - \frac{(n_0 + n_1)}{(n_0 - n_1)^2}\right) + \frac{8n_0}{(n_0 - n_1)^2\sin^2(\vartheta/2)}}\ . \tag{S26}$$

We use for n_0 (n_1) the mean photon number for the $|0\rangle$ ($|1\rangle$) reference curve during each acquisition for different t. On average, $\overline{n_0} \sim 0.0022 \pm 0.0003$ and $\overline{n_1} \sim 0.0015 \pm 0.0002$.

We also consider the fact that the signal $\overline{\mathcal{S}'}$ has contributions from three detunings $\{\delta\omega, A \pm \delta\omega\}$, where A is the hyperfine coupling between the NV center and spin-1 ^{14}N nucleus; taking such detunings into account is, incidentally, fundamental for the choice of interrogation times: given the modulation imposed by the multiple frequencies in the signal, full echo times yielding a high signal amplitude are preferred. In order to compare the ideal sensitivity with the experimental one, in our experiments we need to introduce a further correction factor C_A, since the accumulated phase is only equal to the optimal $\frac{\pi}{2}$ for the experimental realizations with $m_I = 0$. We expect the sensitivity to become larger as $\eta_A = \eta_{M'}/C_A = \eta_M/(C \times C_A)$, with

$$C_A^{-1} = \frac{3}{\left|1 + 2\cos\left(\frac{2At\sin(\vartheta/2)}{\vartheta}\right)\right|}\ . \tag{S27}$$

In order to estimate $C \times C_A$, we use the fitted value for A at each point ($\overline{A} \sim 2\pi \times (2.21 \pm 0.07)$MHz), the time t corresponding to the number of cycles at which the experimental point was taken, and a corrected $\vartheta \sim 0.984\pi$ that takes into account the real angle, given the experimental Rabi frequency, imposed by the duration of the echo half cycle, which can be controlled only up to the inverse of the AWG sample rate. A mean total correction factor of $\overline{C \times C_A} \sim (5.9 \pm 1.4) \times 10^{-3}$ is obtained for the set of points. The mean sensitivity curve (solid line) is expressed as the theoretically expected sensitivity in the absence of noise η_M, divided by $\overline{C \times C_A}$. Similarly, the lower (higher) bounds for the sensitivity are estimated by dividing the theoretical sensitivity by the maximum (minimum) $C \times C_A$ value in the set of points, and are plotted in the dashed blue lines.

We stress that the presence of an unpolarized nitrogen nuclear spin is the sole responsible for the $C_A(t)$ factor. The experimental sensitivity points were thus chosen for times having $C_A(t)$ at a local maximum. The landscape of the quantum magnetometer's expected sensitivity as a function of interrogation time, for an averaged $\overline{C \times C_A(t)}$ that considers the time dependence of $\overline{C_A(t)}$, is shown in red in Supplementary Fig. S3. The data cover the interrogation times where the sensitivity is optimal, even if the effect of the nitrogen nuclear spin were to be corrected for. Polarizing

the nuclear spin [27] or decoupling it with a simple pulse sequence such as a spin echo [6] would remove the effects of the hyperfine coupling and thus set $C_A = 1$. In the experiments, given our careful choice of interrogation times and the estimated hyperfine interaction A, the average over the four points $\overline{C_A} \sim 0.90 \pm 0.13$ is very close to 1.

The effect of decoherence is included in the plot using a fit for $T_2^\star \sim 2.19 \pm 0.15\mu$s from the Ramsey experiment shown in Supplementary Fig. S4.b. Assuming static Gaussian noise, we let $\eta_A \to \eta_A e^{(t/T'_{\rm RE})^2}$, with $T'_{\rm RE} = \frac{T_2^\star \vartheta}{2\sin(\vartheta/2)}$.

Evolution under bath noise

In the presence of Gaussian static noise in the z-direction with variance σ^2, the RE signal decays as

$$\langle \mathcal{S}_{\rm RE} \rangle = \frac{1}{2}\left[1 + \cos^2\left(\frac{\vartheta}{2}\right) + \sin^2\left(\frac{\vartheta}{2}\right)\cos\left(\frac{2\delta\omega t}{\vartheta}\sin\left(\frac{\vartheta}{2}\right)\right) e^{(t/T'_{\rm RE})^2}\right] , \tag{S28}$$

where we define the dephasing time

$$T'_{\rm RE} = \frac{\vartheta}{\sigma\sqrt{2}|\sin(\vartheta/2)|} . \tag{S29}$$

Similarly, one obtains for the Ramsey signal

$$\langle \mathcal{S}_{\rm Ram} \rangle = \frac{1}{2}\left(1 + \cos(\delta\omega t) e^{-(t/T'_{\rm Ram})^2}\right) , \quad \text{with} \quad T'_{\rm Ram} = T_2^\star = \frac{\sqrt{2}}{\sigma} . \tag{S30}$$

Note that $T'_{\rm RE} > T'_{\rm Ram}$ always; nevertheless, at the optimum interrogation time calculated for both sequences as $\frac{T'}{2}$,

$$\frac{\eta_{\rm RE}}{\eta_{\rm Ram}} = \sqrt{\frac{\vartheta}{2\sin(\vartheta/2)^3}} > 1 ; \tag{S31}$$

the sensitivity ratio above has a minimum $\eta_{\rm RE}/\eta_{\rm Ram} \sim 1.20$ for $\vartheta \sim \frac{3\pi}{4}$, which is the angle that yields the highest sensitivity for the RE sequence.

We now turn our attention to the evolution of the Rabi signal under Gaussian dephasing noise. For $\delta\omega \ll \Omega$, the Rabi signal is approximately

$$\mathcal{S}_{\rm Rabi} = 1 - \frac{\Omega^2}{\Omega^2 + \delta\omega^2}\sin^2\left(\frac{t}{2}\sqrt{\Omega^2 + \delta\omega^2}\right) \approx 1 - \left(1 - \frac{\delta\omega^2}{\Omega^2}\right)\sin^2\left(\frac{t}{2}\left(\Omega + \frac{\delta\omega^2}{\Omega}\right)\right) ; \tag{S32}$$

calculating the expected value $\langle \mathcal{S}_{\rm Rabi} \rangle$ under the noise distribution yields

$$\langle \mathcal{S}_{\rm Rabi} \rangle = \frac{1}{2}\left[1 + \frac{\cos(t\Omega + \arctan(t\sigma^2/\Omega)/2)}{\left(1 + \frac{t^2\sigma^4}{\Omega^2}\right)^{\frac{1}{4}}} + \frac{\sigma^2}{\Omega^2}\left(1 - \frac{\cos(t\Omega + 3\arctan(t\sigma^2/\Omega)/2)}{\left(1 + \frac{t^2\sigma^4}{\Omega^2}\right)^{\frac{3}{4}}}\right)\right] . \tag{S33}$$

In the presence of stochastic (Ornstein-Uhlenbeck) noise with zero mean and autocorrelation function $\sigma^2 e^{-\frac{t}{\tau_{\rm c}}}$, a Ramsey signal decays as [39]

$$\langle \mathcal{S}_{\rm Ram} \rangle = \frac{1}{2}\left(1 + e^{-\zeta'(t)}\right) , \quad \text{with} \quad \zeta'(t) = \sigma^2\tau_{\rm c}^2(t/\tau_{\rm c} + e^{-\frac{t}{\tau_{\rm c}}} - 1) . \tag{S34}$$

Numerical simulations valid for $\tau_{\rm c}\sigma \lesssim \vartheta/2$ and $\tau_{\rm c} \gtrsim \vartheta/(2\Omega)$ indicate that the RE signal decays as

$$\langle \mathcal{S}_{\rm RE} \rangle = \frac{1}{2}\left[1 + \cos^2\left(\frac{\vartheta}{2}\right) + \sin^2\left(\frac{\vartheta}{2}\right) e^{-\zeta(t)}\right] , \tag{S35}$$

with

$$\zeta(t) = \zeta'(t)\frac{4\sin^2(\vartheta/2)}{\vartheta^2} . \tag{S36}$$

Note the additional factor $\frac{4\sin^2(\vartheta/2)}{\vartheta^2} = \left(\frac{T'_{\rm Ram}}{T'_{\rm RE}}\right)^2 < 1$.

Simulations that compare different ϑ-RE for $\vartheta = \{3\pi/4, \pi, 5\pi\}$ and Ramsey signals in the presence of stochastic noise are depicted in Supplementary Fig. S5.a; it is clear that RE sequences are more resilient to bath noise with correlation times shorter than the echo period.

Previous calculations [40] indicate that, for slow baths $\frac{1}{\tau_c} \ll \frac{\sigma^2}{\Omega}$, the Rabi signal follows the static noise behaviour for short times, and decays $\propto e^{-\frac{\sigma t}{2\sqrt{\tau_c \Omega}}}$ for long times. Fast baths $\frac{1}{\tau_c} \gg \frac{\sigma^2}{\Omega}$ induce a decay of the Rabi signal $\propto e^{\frac{4\Omega^2}{\sigma^4 \tau_c}}$.

Evolution under excitation field noise

In the presence of a constant error in the Rabi frequency such that $\Omega \to (1+\epsilon)\Omega$, the infidelity $(1-{\rm Tr}[U(\epsilon)U(0)]/2) \equiv (1-F)$ of the pulse sequence is given to second order in the detuning from resonance $\delta\omega$ and in ϵ by

$$(1-F)_{\rm RE} \approx \frac{\epsilon^2 t^2 \delta\omega^2}{8} \frac{(2+\vartheta^2 - 2\cos\vartheta - 2\vartheta\sin\vartheta)}{\vartheta^2} \tag{S37}$$

for RE and

$$(1-F)_{\rm Rabi} \approx \frac{\epsilon^2 t^2 \Omega^2}{8} - \frac{\epsilon^2 \delta\omega^2(-2+t^2\Omega^2+2\cos(t\Omega))}{8\Omega^2} \tag{S38}$$

for Rabi-beat magnetometry.

Similarly, an error in the Rabi frequency will yield a flip-angle error in the Ramsey sequence, resulting in the infidelity

$$(1-F)_{\rm Ram} \approx \frac{\epsilon^2\pi^2}{8} - \frac{\epsilon^2\delta\omega^2(-16+4\pi^2+\pi t\Omega(8+\pi t\Omega))}{32\Omega^2} \ . \tag{S39}$$

In the presence of stochastic noise in the excitation field with zero mean and autocorrelation function $\sigma^2 e^{-\frac{t}{\tau_c}}$, the resonant cases for RE, Rabi have simple analytical solutions.

A cumulant expansion technique applied to periodic Hamiltonians [39, 41] yields for the envelope of a resonant RE sequence

$$\langle \mathcal{S}_{\rm RE} \rangle = \frac{1}{2}\left(1 + e^{-\zeta(n)}\right) \ , \tag{S40}$$

with

$$\zeta(n) = \tau_c^2\sigma^2\left[\frac{2n\vartheta}{\sigma\tau_c} + 2n(e^{-\frac{\vartheta}{\Omega\tau_c}}-1) - \tanh^2\left(\frac{1}{2}\frac{\vartheta}{\Omega\tau_c}\right)\left(2n(e^{-\frac{\vartheta}{\Omega\tau_c}}+1) + e^{-\frac{2n\vartheta}{\tau_c\sigma}} - 1\right)\right] \ . \tag{S41}$$

We note that this decay is equivalent to the decay under pure dephasing for a PDD sequence [42].

In Supplementary Fig. S5.b, we simulate the signal for different ϑ-RE and Rabi sequences if noise in the excitation field is present. Contrarily to RE decay in the presence of bath noise, and as shown experimentally in the main text, RE sequences can refocus excitation noise with correlation times longer than the echo period.

We note that the Rabi signal decay for noise along σ_x should be comparable to Ramsey signal decay in the presence of stochastic noise along σ_z. We thus have the decay

$$\langle \mathcal{S}_{\rm Rabi} \rangle = \frac{1}{2}\left(1 + e^{-\zeta'(t)}\right) \ , \quad \text{with} \quad \zeta'(t) = \sigma^2\tau_c^2(t/\tau_c + e^{-\frac{t}{\tau_c}} - 1) \ . \tag{S42}$$

The advantage of the RE sequence over the Rabi is thus the same advantage that dynamical decoupling sequences can offer.

Repeated readouts

The NV spin state can be read under non-resonant illumination at room temperature using the fact that the $m_S = \pm 1$ excited states can decay into metastable states, which live for ∼300 ns, while direct optical decay happens in about 12 ns. Thus, a NV in the $m_S = 0$ state will emit, and absorb, approximately 15 photons, compared to only a few for a NV in the $m_S = \pm 1$ states, yielding state discrimination by fluorescence intensity. Unfortunately the metastable state decays primarily via spin-non conserving processes into the $m_S = 0$ state thereby re-orienting the spin. This is good for spin polarization, but erases the spin memory and reduces measurement contrast. The detection efficiency C of the NV center spin state is thus given by Eq. S26, which for $\vartheta = k\pi$ reduces to $C = \left(1 + \frac{3(n_0+n_1)}{(n_0-n_1)^2}\right)^{-1/2}$, where $n_{1,0}$ is the number of photons collected if the NV spin is in the $m_S = \{0, 1\}$ state, respectively.

In the repeated readout scheme [27, 43], the state of the nuclear spin is repetitively mapped onto the electronic spin, which is then read out under laser illumination. The measurement projects the nuclear spin state into a mixed state, but the information about its population difference is preserved, under the assumption that the measurement is a good quantum non-demolition measurement. We can include the effect of these repeated readout by defining a new detection efficiency, $C_{N_r} = \left(1 + \frac{1}{N_r}\frac{3(n_0+n_1)}{(n_0-n_1)^2}\right)^{-1/2}$, which shows an improvement $\propto \sqrt{N_r}$, where N_r is the number of measurements. The sensitivity needs of course to be further modified to take into account the increased measurement time. Provided the time needed for one measurement step is smaller than the interrogation time, it becomes advantageous to use repeated readouts. As RE increases the interrogation time, it can achieve better sensitivity than Ramsey magnetometry by using the repeated readout scheme (which is instead not advantageous for a simple Ramsey scheme), as depicted in Supplementary Fig. S6.

Calcium signaling domains

Although virtually all neuronal reactions are regulated by diffusing Ca^{2+} ions between membrane channel sources and cytoplasm target receptors, triggering specificity is ensured by the fact that such diffusion events are localized in time and space. The size of the signaling domain, understood as roughly the distance between channel and receptor (50nm to 0.5μm), determines the diffusion timescale (μs to ms) and strength, the latter measured by Ca^{2+} concentration (100 to 1μM) [29, 44].

Let a flux with duration t and mean travelled distance d between membrane channel and cytoplasm receptor. The magnetic field at a distance r from a transient Ca^{+2} flux composed of l ions is estimated as

$$B(\mathrm{T}) = \frac{\mu_0}{4\pi}\frac{2led}{tr^2} \ , \tag{S43}$$

with e the electron charge, and with the magnetic permeability of the cell approximated by μ_0, the vacuum permeability. Therefore, the minimum required sensitivity to sense the afore-described calcium flux is

$$\eta\left(\frac{\mathrm{T}}{\sqrt{\mathrm{Hz}}}\right) = \sqrt{2\pi}\frac{\mu_0}{4\pi}\frac{2led}{\sqrt{t}r^2}\sqrt{N} \ . \tag{S44}$$

SUPPLEMENTARY REFERENCES

[35] M. Duer, *Introduction to solid-state NMR spectroscopy* (John Wiley & Sons, 2004)

[36] G. L. Bretthorst, *Bayesian spectrum analysis and parameter estimation* (Springer-Verlag, 1988)

[37] D. C. Rife and R. R. Boorstyn, *Single tone parameter estimation from discrete-time observations.* IEEE Transactions on Information Theory **20**, 591–598 (1974)

[38] C. A. Meriles, L. Jiang, G. Goldstein, J. S. Hodges, J. Maze, M. D. Lukin, and P. Cappellaro, *Imaging mesoscopic nuclear spin noise with a diamond magnetometer.* J. Chem. Phys. **133**, 124105 (2010)

[39] R. Kubo, *Generalized cumulant expansion method.* J. Phys. Soc. Jpn. **17**, 1100–1120 (1962)

[40] V. V. Dobrovitski, A. E. Feiguin, R. Hanson, and D. D. Awschalom, *Decay of Rabi oscillations by dipolar-coupled dynamical spin environments.* Phys. Rev. Lett. **102**, 237601 (2009)

[41] P. Cappellaro, J. S. Hodges, T. F. Havel, and D. G. Cory, *Principles of control for decoherence-free subsystems.* J. Chem. Phys. **125**, 044514 (2006)

[42] K. Khodjasteh and D. A. Lidar, *Fault-tolerant quantum dynamical decoupling.* Phys. Rev. Lett. **95**, 180501 (2005)

[43] L. Jiang, J. S. Hodges, J. R. Maze, P. Maurer, J. M. Taylor, D. G. Cory, P. R. Hemmer, R. L. Walsworth, A. Yacoby, A. S. Zibrov, and M. D. Lukin, *Repetitive readout of a single electronic spin via quantum logic with nuclear spin ancillae.* Science **326**, 267–272 (2009)

[44] B. Fakler and J. P. Adelman, *Control of K_{Ca} channels by calcium nano/microdomains.* Neuron **59**, 873–881 (2008)